ADVANCED MATERIALS
www.advmat.de

Spin-Selective Memtransistors with Magnetized Graphene

Juyeong Jeong, Do Hoon Kiem, Dan Guo, Ruihuan Duan, Kenji Watanabe, Takashi Taniguchi, Zheng Liu, Myung Joon Han, Shoujun Zheng,* and Heejun Yang**

Spin-polarized bands in pristine and proximity-induced magnetic materials are promising building blocks for future devices. Conceptually new memory, logic, and neuromorphic devices are conceived based on atomically thin magnetic materials and the manipulation of their spin-polarized bands via electrical and optical methods. A critical remaining issue is the direct probe and the optimized use of the magnetic coupling effect in van der Waals heterostructures, which requires further delicate design of atomically thin magnetic materials and devices. Here, a spin-selective memtransistor with magnetized single-layered graphene on a reactive antiferromagnetic material, CrI_3, is reported. The spin-dependent hybridization between graphene and CrI_3 atomic layers enables the spin-selective bandgap opening in the single-layered graphene and the electric field control of magnetization in a specific CrI_3 layer. The microscopic working principle is clarified by the first-principles calculations and theoretical analysis of the transport data. Reliable memtransistor operations (i.e., memory and logic device-combined operations), as well as a spin-selective probe of Landau levels in the magnetized graphene, are achieved by using the subtle manipulation of the magnetic proximity effect via electrical means.

1. Introduction

Spin manipulation is considered a promising approach for developing energy-efficient, fast, and highly integrated nonvolatile memory and logic devices, and to extend potential application to neuromorphic technologies.[1–3] Recent spintronic devices with low-dimensional magnetic materials and their interfaces have demonstrated original spin injection, flip, and detection.[4–8] Spin transfer torque and spin-orbital torque have been already adopted at the industrial level for memory devices,[9–11] and novel materials are being continuously pursued to achieve higher performance. Atomically thin magnetic materials and dielectric media have been suggested and investigated for practical device applications, employing versatile spin manipulation techniques.[12–16]

Layered magnetic and semiconducting materials,[17,18] represented by CrI_3,[14,19] $CrBr_3$,[20] and $Cr_2Ge_2Te_6$,[14,20] have exhibited variable layer-by-layer magnetic orderings that can be controlled using electrical methods.[8,21,22] Electric control of the magnetic features of van der Waals (vdW) heterostructures comprised of layered magnetic materials has been demonstrated, with key mechanisms based on magnetoelectric (ME) effects and electrostatic (ES) effects.[20,22,23] In contrast to optical probes of the ME effect in vdW heterostructures,[21] tunneling current modulation in a vertical vdW heterostructure of multilayered graphene/CrI_3/graphene is considered to be compatible with practical memory technology. In this approach, spin-polarized tunneling current occurs due to the variable interlayer magnetic orderings, and the resulting tunnel barriers in the CrI_3.[24–26]

Critical issues remain for novel device operation, including a direct probe, and the optimized use of the delicate interactions (i.e., magnetic proximity) in the magnetic vdW systems. For example, while former theoretical studies[27–29] have suggested that a graphene monolayer on CrI_3 can exhibit intriguing magnetic properties, such as spin-polarized band hybridization with valley splitting,[30] giant tunneling magnetoresistance,[31] and Chern insulating state,[32] experimental demonstrations have been lacking. Moreover, further investigations of the major physical origins of phenomenologically-treated ME and ES effects are of crucial importance for the control of atomically thin magnetized materials and the optimized design of delicate spintronic devices based on vdW heterostructures.

J. Jeong, D. H. Kiem, M. J. Han, H. Yang
Department of Physics
Korea Advanced Institute of Science and Technology (KAIST)
Daejeon 34141, South Korea
E-mail: mj.han@kaist.ac.kr; h.yang@kaist.ac.kr

D. Guo, S. Zheng
Centre for Quantum Physics
Key Laboratory of Advanced Optoelectronic Quantum Architecture and Measurement (MOE)
School of Physics, Beijing Institute of Technology
Beijing 100081, China
E-mail: szheng@bit.edu.cn

R. Duan
CINTRA CNRS/NTU/THALES
Research Techno Plaza
Nanyang Technological University
Singapore 637371, Singapore

R. Duan, Z. Liu
School of Materials Science and Engineering
Nanyang Technological University
Singapore Singapore

K. Watanabe, T. Taniguchi
International Center for Materials Nanoarchitectonics
National Institute for Materials Science
1-1 Namiki, Tsukuba 3030044, Japan

The ORCID identification number(s) for the author(s) of this article can be found under https://doi.org/10.1002/adma.202310291

DOI: 10.1002/adma.202310291

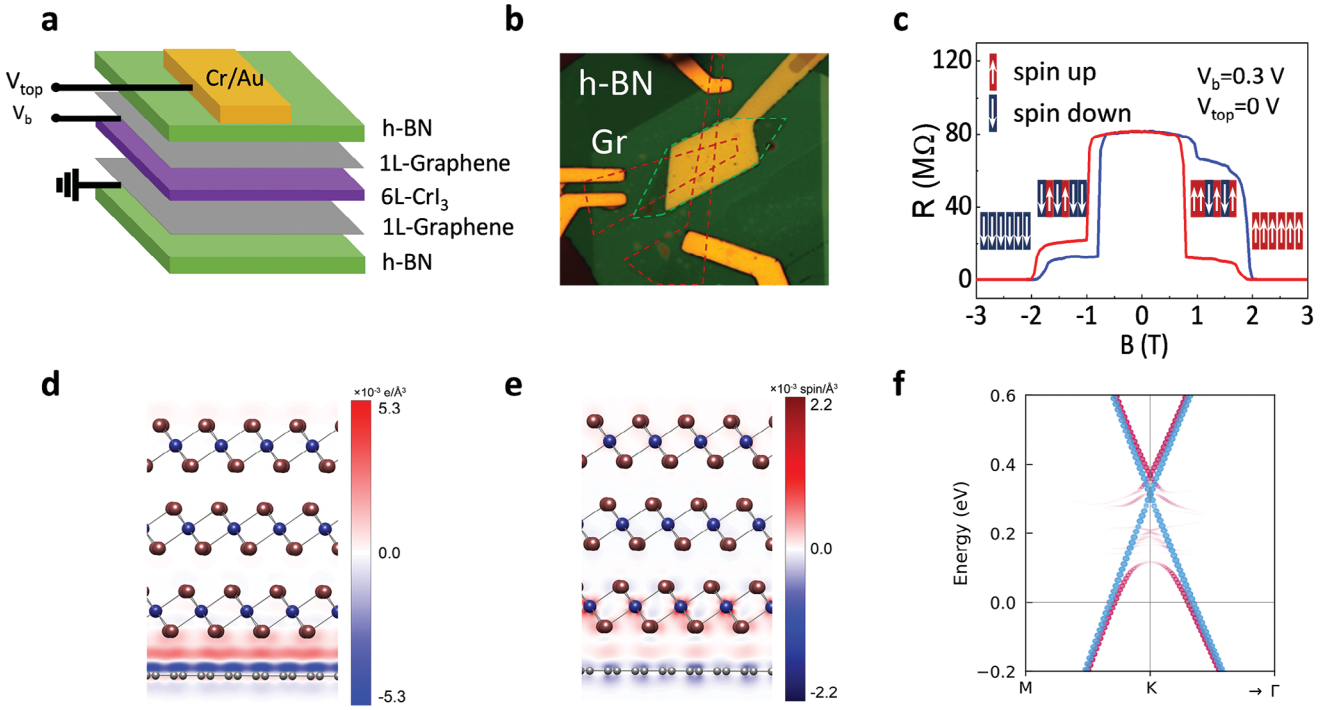

Figure 1. Spin-dependent band hybridization in graphene on CrI_3. a) Schematic of our memtransistor based on a structure of 1L-graphene/6L-CrI_3/1L-graphene. b) An optical microscope image of our memtransistor. c) Tunneling resistance as a function of the applied magnetic field, exhibiting spin flip in the CrI_3 layers. d) The DFT-calculated charge density difference plot $\Delta\rho = \rho_{total} - \rho_{CrI_3} - \rho_{graphene}$, where the colormap shows the averaged value of $\Delta\rho$ on the (100) plane. Blue, brown, and grey spheres represent Cr, I, and C atoms, respectively. e) The DFT-calculated spin density difference, where the blue and red colors show the majority and minority spin density, respectively. f) The calculated band dispersion of the graphene/CrI_3 heterostructure. The red and blue dots show the graphene-projected components with up and down spin, respectively. Their dot size and color intensity indicate the magnified projection ratio.

Numerous studies have been conducted on vertical/lateral CrI_3 heterostructures, primarily concentrating on the modulation of spin arrangements in CrI_3 through diverse means such as magnetic fields, gate voltages, and pressure application.[25,26,33] These investigations predominantly emphasize the characteristics of CrI_3 rather than graphene. Additionally, several studies have delved into graphene properties such as the opening of band gaps in bilayer graphene /CrI_3 or the occurrence of anomalous Landau levels (LLs) in graphene on CrI_3.[34,35] Despite these efforts, the intricate mechanisms underlying band hybridization in monolayer graphene/CrI_3 heterostructure are yet to be fully elucidated.

In this study, we demonstrate a spin-selective memtransistor with a magnetized graphene monolayer on CrI_3. It reflects a device-scale, direct, and spin-selective probe and the use of exchange interactions in the vdW heterostructure system. In particular, transport measurements of our memtransistor reveal a spin-selective bandgap opening in the magnetized graphene, originating from spin-polarized band hybridization with the reactive antiferromagnetic CrI_3. The spin-selective band hybridization generates spin-polarized LLs in the graphene under magnetic fields, uniquely measured by the spin-dependent tunneling current in our memtransistor.

Our first-principles calculations and further theoretical analysis clarified the working mechanism of our memtransistor; the interlayer exchange interactions can be modulated via spin-dependent charge transfer between the graphene and CrI_3, which can be used to manipulate the antiferromagnetic interaction and induce spin flip across the CrI_3 layers via electric interaction.

2. Results and Discussion

2.1. Spin-Selective Band Hybridization in Graphene on CrI_3

The structure of our memtransistor is based on a vdW heterostructure of monolayer graphene/six layers of CrI_3 /monolayer graphene and is schematically shown in **Figure** 1a. An optical image of the memristor showing the geometry of electrodes and channel materials is provided in Figure 1b. The two monolayer graphene layers, susceptible to the reactive CrI_3 layers, act as electrodes for spin-polarized tunneling currents.

The edges of two graphene flakes were manually aligned to generate resonant tunneling in terms of the momentum and spin of the tunneling electrons. We chose single-layered graphene layers and reactive CrI_3 as the electrodes and tunneling barrier in the vdW structure, respectively, so that the proximity-induced magnetization in graphene and the band hybridization at the interface could be maximized. It has been reported that the proximity effect between single-layered graphene and CrI_3 determines the spin-selective tunneling barrier heights.[34]

Magnetic field-dependent tunneling current in the memtransistor is shown in Figure 1c, where two thresholds of magnetic fields are observed: B = 0.8 and 2 T. In former studies, two

threshold values have been reported with multilayered graphene and CrI_3,[24,25] which are subject to spin rearrangement in CrI_3 layers. As discussed below in detail, we attribute the smaller threshold field (0.8 T) to the easier spin flip of the outermost CrI_3 layer in direct contact with the graphene. The inner layer spin reversal, however, requires a higher magnetic field because of the stronger interlayer exchange interaction, resulting in the threshold value of $B = 2$ T. The antiferromagnetic inter-layer interactions of CrI_3, which can be modified by the graphene contact in addition to its intrinsic nature, are key to understanding the electric field-induced spin flip in our spin-selective memtransistor.

First-principles calculations provide useful insights into understanding the working principle of our memtransistor. Due to their different electron affinity, charge transfer occurs at the graphene-CrI_3 interface. Figure 1d shows a plot of the charge distribution difference across the graphene-CrI_3 interface. It is clearly noted that the electrons are depleted (blue-colored clouds) in the graphene and accumulated (red-colored clouds) in the CrI_3; the transferred electrons reside mostly around the iodine ions in CrI_3 (represented by brown-colored spheres).

The transferred charges are spin-polarized. While bare graphene is spin-unpolarized, electrons whose spin direction is identical to those in the adjacent atomic layer of CrI_3 are selectively transferred from the graphene to CrI_3. Accordingly, the interfacial graphene becomes polarized with the opposite spin. The spin density difference plot in Figure 1e shows that graphene becomes polarized with down spin (blue-colored), while the interfacial CrI_3 gains more up-spin electrons (red-colored).

The corresponding band structure of the magnetized graphene is presented in Figure 1f, where red and blue circles represent up- and down-spin bands, respectively. The energy position of Dirac points is located above the chemical potential by ≈0.3 eV, which is consistent with the observed charge transfer and the following LL measurements. The graphene bands become spin-dependent in proximity to the magnetic CrI_3 layers; the up-spin band (red-colored bands) is significantly deformed from the original linear feature and the low-lying parabolic band forms a hole pocket at the K point. On the other hand, the down-spin band (blue-colored) retains its original linear dispersion around the Dirac point. The spin-dependent band deformation originates from the spin-dependent electron transfer to CrI_3. The spin-selective hybridization opens an energy gap only for the majority (up) spin band while keeping the original gapless linear Dirac dispersion for the minority (down) spin band. Unlike most other magnetic substrates that can also induce spin-polarization of graphene, the aforementioned features are quite distinct, particularly, the spin-selective gap opening.[36,37]

2.2. Tunneling Transport with Spin-Polarized Bands of Graphene on CrI_3

The two single-layered graphene electrodes and the tunneling barrier of six CrI_3 layers in our spin-selective memtransistor exhibit nonlinear current–voltage (I–V_b) curves as shown in **Figure 2a**. The tunneling currents can be substantially modulated by the top gate voltage (V_{top}); the Fermi level of the single-layered graphene can be easily shifted by V_{top}. The magnified I–V_b curves in the inset of Figure 2a clearly show the modulation of the tunneling currents. However, the tunneling current modulation in Figure 2a demonstrates nonmonotonic current changes, which cannot be simply explained by the doping (gating) and the presence of the Dirac point of the graphene.

To better show the nonmonotonic current changes, a transfer curve (I–V_{top}) of the device with $V_b = -0.3$ V is shown in Figure 2b. In contrast to the bilayer graphene/CrI_3/bilayer graphene heterostructure devices, which exhibit a distinct gap-assisted feature,[26,38] the transfer curve of the monolayer graphene/CrI_3/monolayer graphene heterostructure displays the pronounced V-shape transfer curve behaviors as a function of V_{top} attributed to spin-selective gap opening (Figure 2b). We have included absolute current values in Figure 2a, to avoid polarity-related misunderstanding of the novel current feature.

The nontrivial feature of the transfer curves in Figure 2b could be further analyzed theoretically. The calculated tunneling probability based on the spin-dependent DFT band structure is presented in Figure 2c. The bottom graphene layer (b-Gr) is grounded and electrons tunnel from the top graphene layer (t-Gr) with $V_b = -0.3$ V. The band diagrams corresponding to two different regimes of V_{top} (i.e., "I" and "II" in Figure 2b) are shown in Figure 2d,e with the higher potential energy electrons in t-Gr (by $V_b = -0.3$ V). The Fermi level difference between b-Gr and t-Gr is set to $|V_b|$. Since an even number of layers (six layers) of CrI_3 are used in our device, t-Gr and b-Gr layers are polarized with opposite spins as demonstrated by the asymmetric feature of two band diagrams corresponding to b-Gr (left side) and t-Gr (right side).

Two critical factors determine the nontrivial tunneling transport: 1) the gate-driven tunneling barrier height change and 2) the spin-selective bandgap opening in graphene. First, the gate voltage modulates both graphene Fermi level and CrI_3 barrier height via their relative band alignment.[39,40] For example, a positive V_{top} accumulates electrons in t-Gr, which raises the Fermi level in t-Gr, and simultaneously, decreases the tunneling barrier in CrI_3. Thus, the current increases with V_{top} as observed in the range "I" (Figure 2b), which can be explained by the reduced tunneling barrier at higher V_{top}. This character is well captured by our simulation; see the green line in Figure 2c.

The range "II" is marked by the sudden decrease of the current (see Figure 2b), which cannot be explained simply by the barrier height change. Here we note that the reduced density of states in t-Gr (as its Fermi level approaches to Dirac point) cannot explain this decrease either because the Dirac point is located at around $V_{top} = 12$ V in our memtransistor. Accordingly, we need to take into account the spin-selective bandgap opening in graphene.

The tunneling currents can be described as follows

$$I\left(V_{top}\right) = \int_0^{|V_b|} N_{top}\left(E, V_{top}\right) T\left(E, V_{top}\right) N_{bottom}\left(E, V_{top}\right) dE \quad (1)$$

where $N_{top/bottom}(E,V_{top})$ is the density of states of t-Gr/b-Gr, and $T(E,V_{top})$ is the tunneling transmission coefficient. We note that $N_{top/bottom}$ should involve only mobile electrons with proper band dispersion (group velocity). We obtained $N_{top/bottom}(E,V_{top})$ from our first-principles calculations while $T(E,V_{top})$ can be derived from Wentzel–Kramers–Brillouin (WKB) approximation

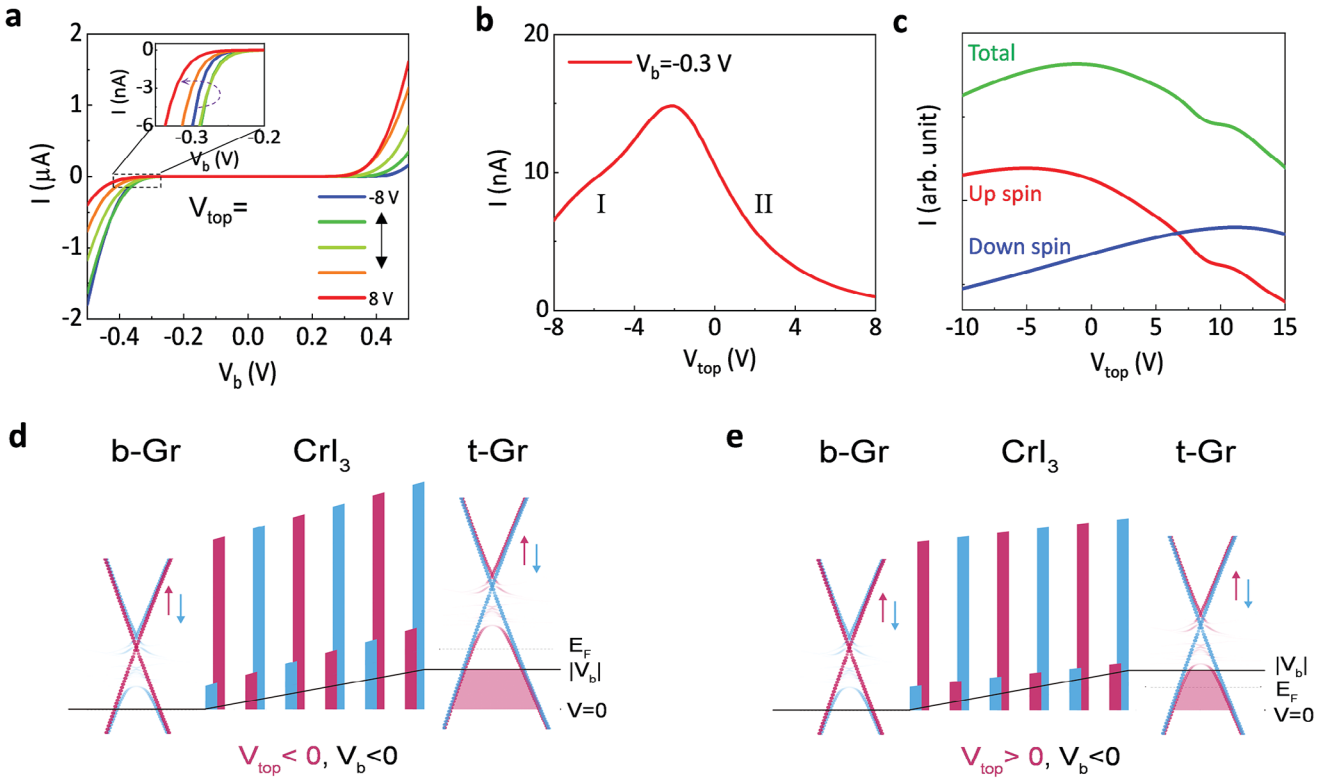

Figure 2. Tunneling transport and bandgap opening in graphene on CrI_3. a) The tunneling current as a function of V_b at various V_{top} values. The inset magnifies the tunneling current marked by the dashed box. b) Transfer curve with $V_b = -0.3$ V. c) Calculated transfer curves, decomposed by the spin of electrons. The red and blue curves indicate up and down spin components of the tunneling current from the graphene. The green curve shows the total tunneling current, which corresponds to the transfer curve in (a). d,e) Two band diagrams of the channel in our memtransistor, corresponding to the two V_{top} ranges ("I" and "II") marked in (b). The barrier heights decrease as the t-Gr becomes more n-doped by increasing V_{top} (d). The Fermi level of t-Gr approaches the bandgap energy as we further increase V_{top} (e).

(see Figures S9 and S10, Supporting Information, for more details).

The red and blue curve in Figure 2c shows up- and down-spin contributions, respectively, to the tunneling current. The down spin current component (minority spin, blue curve) increases as we increase V_{top} up to $V_{top} = 10$ V. This is consistent with the observed trend that the lower tunneling barrier produces the larger current in the regime of "I" (see Figure 2b). On the other hand, the up-spin current (majority spin, red curve) exhibits a peak at a negative V_{top}. Thus, the total tunneling current (green curve in Figure 2c) qualitatively well reproduces our nontrivial tunneling current profile shown in Figure 2b. It is noteworthy that the spin-selective band gap opening of the single-layer graphene is experimentally confirmed by the band hybridization with a magnetic vdW material.

2.3. Spin-Polarized Landau Levels in Graphene on CrI_3

To further investigate the spin-selective bandgap opening in graphene, the LLs in the t-Gr layer were measured under vertical magnetic fields (>2 T). We note that the high magnetic field aligns all the spins in CrI_3, and therefore, the CrI_3 layers become ferromagnetic. Accordingly, only the majority spin (i.e., parallel to the spin direction in CrI_3) electrons in the graphene can efficiently penetrate the six CrI_3 layers with a lower tunneling barrier height.[18,41] The tunneling transport allows us to measure the LLs formed only in the majority spin-polarized band of the graphene (t-Gr), while the other spin current is blocked by a higher tunneling barrier.

Two transconductance (dI/dV_{top}) mappings (or Landau fan diagrams) of our memtransistor are shown in **Figures** 3a,b with $V_b = -0.2$ and +0.2 V, respectively, as a function of magnetic field (y-axis) and V_{top} (x-axis). We overlaid the transfer curves (shown in Figure 2) with the transconductance mappings in Figure 3 to see the effect of the spin-selective bandgap opening on the LL formation. The range of V_{top} for the red ("Region 1" in Figure 3a) and the blue background regions ("Region 2" in Figure 3a) of transconductance matches the transfer curve with the positive ("range I") and negative ("range II") slopes in Figure 2b, respectively.

As the LL stripes of transconductance pass the peak of the transfer curve (black overlaid curve) and approach the Dirac point ($V_{top} \approx +12$ V), clear nonlinearity appears in the Landau fan diagram (Figure 3a,b). The slope of LL stripes in "Region 2," corresponding to the hybridized band energy range in the graphene, is found to be smaller than that in "Region 1,", which corresponds to the linear band dispersion energy range in the graphene. The nonlinearity indicates the presence of band renormalization and massive Dirac fermions at the CrI_3/graphene interface, induced

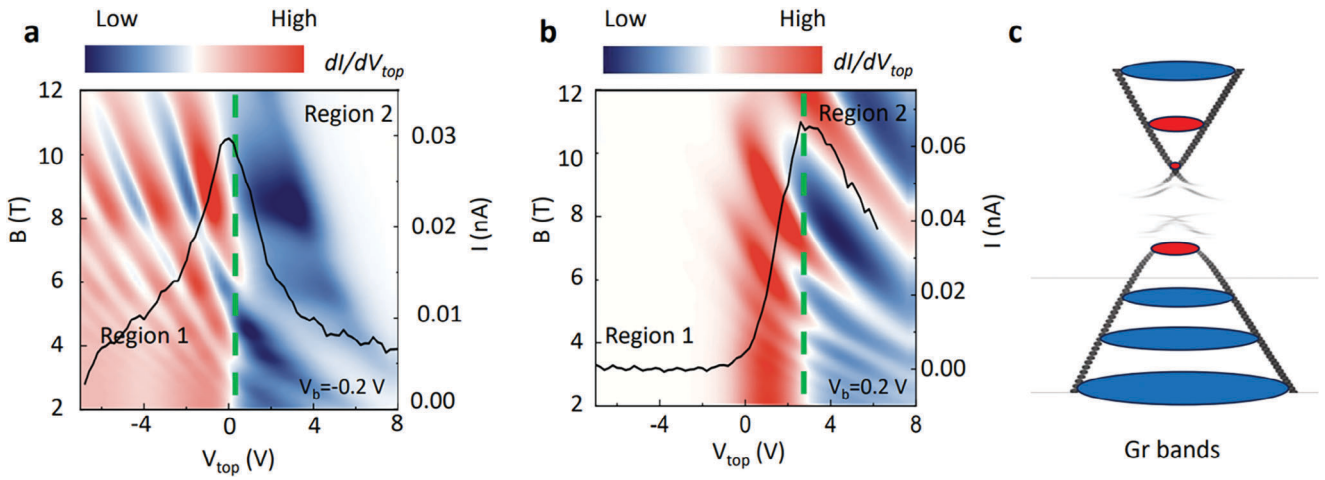

Figure 3. Spin-polarized LLs in graphene on CrI_3. dI/dV_g maps as a function of V_{top} and magnetic field with a) $V_b = -0.2$ V and b) $V_b = 0.2$ V. Clear LL stripes are shown in the dI/dV_g maps, where different slopes of LLs appear in the two regions (Region 1 and 2). The LLs in Region 1 are generated in the linear band dispersion of graphene, while the LLs in Region 2 are produced by the hybridized spin-selective bands. The slope change of LLs across the green vertical dotted line indicates different LL formations in the t-Gr by the hybridized bands in the t-Gr with CrI_3. c) Schematic LLs in the magnetized graphene on CrI_3. The black dotted lines depict the hybridized spin band for the graphene on CrI_3. The red circles indicate the LLs in the massive Dirac dispersion, whereas the blue circles show the LLs in the pristine graphene with the non-hybridized linear dispersion.

by the reciprocal spin-charge coupling effect in the vdW heterostructure.

The nonlinear slope change in the LL stripes proves the graphene band modification by spin-dependent charge transfer and induced-spin charge coupling, which have been vaguely called ME and ES effects. We note that a similar phenomenon has been interpreted as a gating effect of CrI3.[33] But the current peak in the transfer curve and its coincidence with the boundary of the nonlinearity in Regions 1 and 2 support our claim on the band hybridization effect. As the Fermi level is located close to the band edge, the quadratic graphene band dominates the transport and produces the different intervals of LLs (shown as red and blue lines in Figure 3c), demonstrating the nonlinear feature in the Landau fan diagram.

2.4. Electric Controls of the Spin-Selective Memtransistor

The unique proximity effect in graphene/CrI_3 enabled us to develop a spin-selective memtransistor with magnetized graphene. Despite the interlayer antiferromagnetic ordering in pristine CrI_3, the contact with graphene and the resulting spin-selective charge transfer can modulate the critical magnetic field for spin flip in the adjacent CrI_3 layer. As a result, we fabricated a device (Figures S3 and S4, Supporting Information) and investigated the electrostatic manipulation of the CrI_3 spin orientation at the interface.

The I–V_{top} hysteresis curves are clearly observed as shown in **Figure** 4a which summarizes the results of three magnetic fields close to the first threshold value of spin-flip (0.8 T). We can define the "gate (V_{top}) threshold" that induces the abrupt current change. It exhibits a linear relationship with the applied magnetic field from which the zero-field value is estimated to be 45 V for spin-flip (see the y-intercept in Figure 4b).

The abrupt current change is driven by V_{top} in Figure 4a, which we attribute to the spin-flip in the outermost interface layer of CrI_3 (also shown in Figure 1c) by V_{top}. In Figure 4c, however, we observe that the critical V_{top} for spin flip is hardly changed by V_b. Namely, the spin-flip dynamics at the interface are mostly affected by the charge transfer, that is modulated by V_{top}, rather than the electric field effect through the CrI_3 with a current flow generated by V_b.

Similar phenomena have been reported as ME effects, which mainly focused on memristive effect or charge transfer phenomena.[21–23,42] However, the roles of memtransistor, charge transfer (V_{top}), interfacial graphene, and electric field (V_b), as well as their microscopic mechanisms, remained unclear. Even though the previous theoretical studies revealed the hybridization of the CrI_3/graphene interface, its impacts on the magnetic coupling have not been well understood.[30–32,34]

To gain a detailed understanding and a deeper insight into the proximity effect, we performed first-principles calculations based on density functional theory.[43–45] The results of the interlayer exchange interaction (J^{inter}) are presented in Figure 4d. Two distinctive layer-layer interactions, J_{12} (between the outer-most and the adjacent CrI_3 layer) and J_{23} (between two inner layers of CrI_3), are compared as a function of carrier density. See also Figure 4e for a schematic representation of J_{12} and J_{23}. The contact with graphene induces a notable change in CrI_3. As shown in Figure 4d, both J_{12} and J_{23} exhibit an antiferromagnetic nature, but their strengths are substantially different even at zero doping ($\Delta = 0$). The outer layer coupling (J_{12}) is smaller than the inner (J_{23}), which is attributed to the interface effect in proximity to the graphene. This implies that the outer layer spin order can be reversed easier to be ferromagnetic by the weaker magnetic field. It is consistent with our experimental results (Figures 1c and 4a).

It is interesting to note that the calculated J_{12} corresponds to ≈0.4 T which is similar to the experimental value of 0.8 T. In addition, J_{12} becomes negative at $\Delta = 10$ meV (scaled by a Fermi

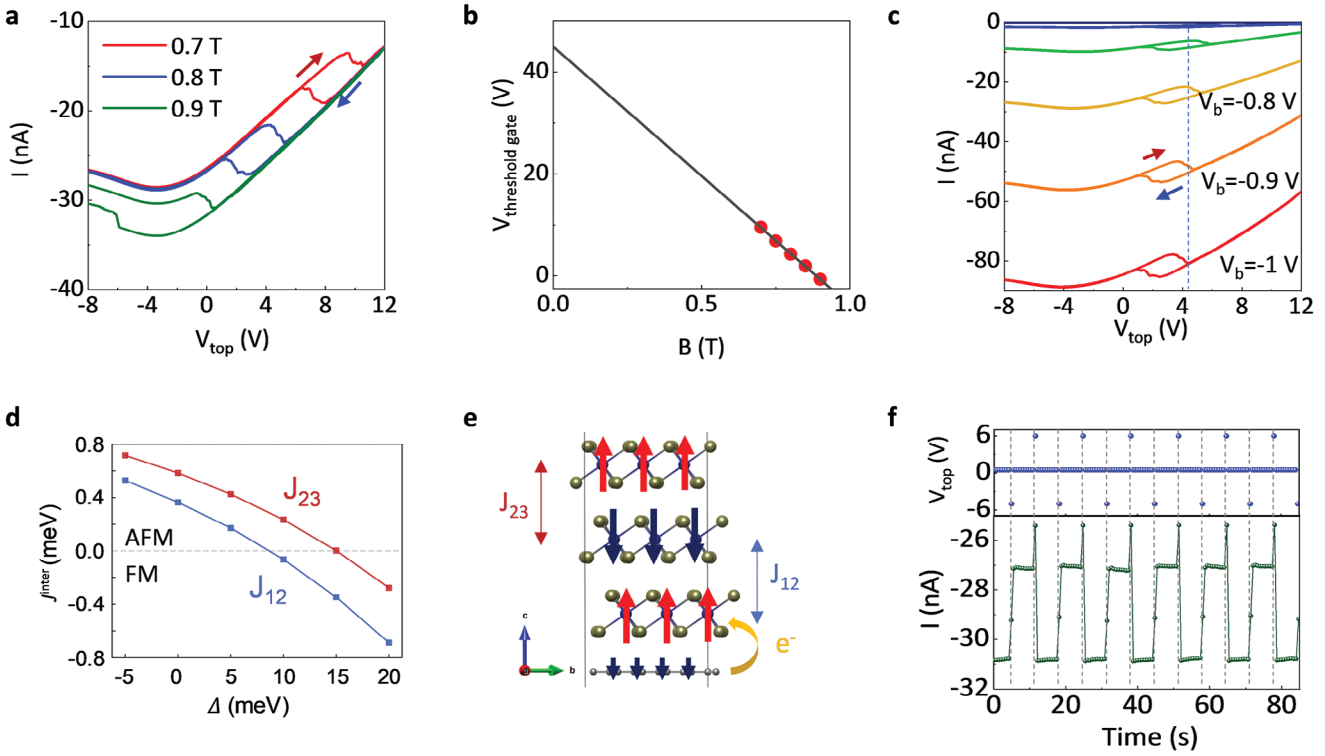

Figure 4. Spin-selective memtransistors. a) I–V_{top} curves with magnetic fields of 0.7, 0.8, and 0.9 T, which show the electric control of spin-flip in our spin-selective memtransistor. A higher V_{top} is required to trigger the spin-flip with a lower magnetic field. b) Extrapolation of threshold V_{top} as a function of the magnetic field, showing a linear relationship. c) I–V_{top} curves at various V_b, indicating the spin-flip is dominated by V_{top}. d) The calculated results of doping-dependent interlayer exchange interactions. The net interactions J^{inter} are given by the sum of interactions between the Cr ions of different layers. e) A schematic picture of the reduced antiferromagnetic interlayer coupling caused by charge transfer. f) Reliable memtransistor operation by V_{top} pulses. Write, read, and erase operations could be achieved by the V_{top} pulses.

level shift by 10 meV), indicative of the zero-field spin flip. The J_{23} also becomes negative at $\Delta = 15$ meV, and therefore beyond this value, the entire CrI_3 can become ferromagnetic solely by doping. Thus, the graphene contact allows easier control of the magnetic ordering in the layered magnetic material (CrI_3), as well as the magnetized graphene (reciprocal effect). The abrupt change in current in Figure 4a reflects the contact effect.

The original magnetic ordering control enables the operation of our spin-selective memtransistor in Figure 4f. We applied V_{top} pulses with amplitudes of +6 and −6 V which can switch the memory states (conductance) in Figure 4f. The modified charge transfer by V_{top} pulses manipulates the nonvolatile and spin-dependent tunneling barrier height (known as the ME effect in former studies) by engineering the spin-polarized band of the t-Gr under $B = 0.8$ T. The reliable spin flips and memory states in Figure 4f prove the modulation of spin-selective charge transfer between graphene and CrI_3, which is further supported by our theoretical study.

3. Conclusions

We developed a spin-selective memtransistor, where spin-polarized tunneling currents reflect the reciprocal magnetic proximity effect between single-layered graphene and CrI_3. Our experiment, as evidenced by the transfer curve and fan diagram along with theoretical results of spin-dependent charge transfer and spin-selective band hybridization, has revealed the magnetization of graphene. A spin-polarized bandgap opening in the magnetized graphene and tunneling barrier height could be demonstrated at various electric and magnetic fields in the memtransistor. In particular, the major role of spin-selective charge transfer (that can be modulated by electrical methods) for the control of the spin configuration in CrI_3 has been explained by our first-principles calculations. Our study paves the way for controlling effective proximity effects in vdW magnetic heterostructures, providing a new route for next-generation memory and logic devices based on spin operation.

4. Experimental Section

Spin-Selective Memtransistor Fabrication: Bulk CrI_3 single crystals were synthesized via the chemical vapor transport (CVT) method. Cr powder with a bit of excess I_2 was loaded into a silica tube, which was sealed under a high vacuum ($<10^{-2}$ Pa). Then, the sealed tube was put in a two-zone furnace, whose reaction and growth zones were heated to 650 and 550 °C, respectively. After 7 days, bulk CrI_3 crystals were obtained in the growth zone. The graphene/CrI_3/graphene vdW devices were fabricated via the dry-transfer method in a glovebox under an Ar atmosphere. A polycarbonate (PC) film was used to pick up a thick h-BN flake, which was used to not only pick up the rest of the graphene/CrI_3/graphene structure but also a dielectric layer for the top gate. Also, the same monolayer graphene flake was used as both the top and bottom electrodes to avoid lattice misorientation. Another h-BN flake was put on the bottom of the whole device

to protect the CrI_3 from degradation. The PC film with the heterostructure was released on the new Si/SiO_2 substrate and the PC was washed with the Chloroform solvent.

The samples were prepared for electrode fabrication by standard electron beam lithography. Graphene edge contacts were fabricated by reactive ion etching with an O_2/SF_6 mixture (10/10 sccm) with a power of 50 W for 20 s. After RIE, Cr/Au (5/50 nm) film was directly deposited on the patterned samples. To prepare the top gate, another set of EBL was prepared.

Sample Characterizations and Transport: All optical images were taken with a Nikon Eclipse LV100 optical microscope. The spin tunneling devices were loaded in an Oxford instruments cryostat (temperature range of 1.5–300 K and magnetic field range of 0–12 T) for temperature and magnetic field sweep measurements. Bias and gate voltage were applied to our devices by a Keithley 4200 SCS system to obtain the tunneling current. All the transport measurements in this manuscript were conducted at $T = 1.5$ K.

Computational Methods: First-principles calculations were carried out within density functional theory as implemented in the "OpenMX" software package.[46] The generalized gradient approximation (GGA) with Perdew–Burke–Ernzerhof (PBE) was used for the exchange-correlation functional.[47] The vdW interactions were considered with the vdW-D3 functional[48,49] and consistent results with vdW-D2 were also obtained.[50] The strong on-site correlation effects of the Cr 3*d* electrons were taken into account with the so-called "fully localized limit (FLL)" of charge-dependent GGA+U (or cDFT+U).[51–55] $U = 2.9$ eV and $J_H = 0.7$ eV were adopted as obtained from constrained random approximation (cRPA) values, as used in previous studies.[45,56] A $9 \times 9 \times 1$ k-mesh was used, and the lattice parameters, as well as the internal coordinates, were optimized with a force criterion of 10^{-2} eV $Å^{-1}$. The magnetic exchange interactions were calculated by magnetic force linear response calculation[57] implemented in the Jx package.[58–62]

Supporting Information

Supporting Information is available from the Wiley Online Library or from the author.

Acknowledgements

This work was supported by the Samsung Research Funding & Incubation Center of Samsung Electronics, under project no. SRFC-MA1701-52. The authors thank support from the Natural Science Foundation of China grant (12 104 050) and the Beijing Institute of Technology Research Fund Program for Young Scholars. This work was supported by the National Research Foundation of Korea (NRF) grant funded by the Korea government (MSIT) (No. 2021R1A2C1009303) and by the Korea Basic Science Institute (KBSI) National Research Facilities & Equipment Center (NFEC) grant funded by the Korea government (Ministry of Science and ICT) (NO.PG2022004-09).

Conflict of Interest

The authors declare no conflict of interest.

Author Contributions

J.J. and D.H.K. contributed equally to this work. S.Z. and J.J. fabricated all the devices and obtained the data. D.G., R.D., and Z.L. synthesize CrI_3 bulk samples. K.W. and T.T. synthesized h-BN samples. D.H.K. performed the first-principles calculation and theoretical analysis under the supervision of M.J.H. H.Y. is the principal investigator and supervised the project. All authors participated in scientific discussions and contributed to the manuscript.

Data Availability Statement

The data that support the findings of this study are available from the corresponding author upon reasonable request.

Keywords

CrI_3, magnetized graphene, memtransistor

Received: October 5, 2023
Revised: December 8, 2023
Published online:

[1] I. M. Miron, K. Garello, P.-J. Zermattern, M. V. Costache, S. Auffret, S. Bandirera, B. Rodmacq, A. Schuhl, P. Gambardella, *Nature* **2011**, *476*, 189.
[2] P. Wadley, *Nat. Mater.* **2018**, *17*, 566.
[3] X. Cheng, Z. Cheng, C. Wang, M. Li, P. Gu, S. Yang, Y. Li, K. Watanabe, T. Taniguchi, W. Ji, L. Dai, *Nat. Commun.* **2021**, *12*, 6874.
[4] S. C. Baek, V. P. Amin, Y. Oh, G. Go, S. Lee, G. Lee, K. Kim, M. D. Stiles, B. Park, K. Lee, *Nat. Mater.* **2018**, *17*, 509.
[5] A. Soumyanarayana, N. Reyren, A. Fert, C. Panagopoulos, *Nature* **2016**, *539*, 509.
[6] E. J. Telford, A. H. Dismukes, R. L. Dudely, R. A. Wiscons, K. Lee, D. G. Chica, M. E. Ziebel, M. Han, J. Yu, S. Shabani, A. Scheie, K. Watanabe, T. Taniguchi, D. Xiao, Y. Zhu, A. N. Pasupathy, C. Nuckolls, X. Zhu, C. R. Dean, X. Roy, *Nat. Mater.* **2022**, *21*, 754.
[7] Z. Qiu, M. Holwill, T. Olsen, P. Lyu, J. Li, H. Fang, H. Yang, M. Kashchenko, K. S. Novoselov, J. Lu, *Nat. Commun.* **2021**, *12*, 70.
[8] X. Wang, J. Tang, X. Xia, C. He, J. Zhang, Y. Liu, C. Wan, C. Fang, C. Guo, W. Yang, Y. Guang, X. Zhang, H. Xu, J. Wei, M. Liao, X. Lu, J. Feng, X. Li, Y. Peng, H. Wei, R. Yang, D. Shi, X. Zhang, Z. Han, Z. Zhang, G. Zhang, G. Yu, X. Han, *Sci. Adv.* **2019**, *5*, eaaw8904.
[9] A. Soumyanarayanan, N. Reyren, A. Fert, C. Panagopoulos, *Nature* **2016**, *539*, 509.
[10] I. M. Miron, G. Gaudin, S. Auffret, B. Rodmacq, A. Schuhl, S. Pizzini, J. Vogel, P. Gambardella, *Nat. Mater.* **2010**, *9*, 230.
[11] J. Železný, P. Wadley, K. Olejník, A. Hoffmann, H. Ohno, *Nat. Phys.* **2018**, *14*, 220.
[12] L. Liu, C. Pai, Y. Li, H. W. Tseng, D. C. Ralph, R. A. Buhrman, *Science* **2012**, *336*, 555.
[13] H. An, T. Ohno, Y. Kanno, Y. Kageyama, Y. Monnai, H. Maki, J. Shi, K. Ando, *Sci. Adv.* **2018**, *4*, eaar2250.
[14] B. Huang, G. Clark, E. Navarro-Moratalla, D. R. Klein, R. Cheng, K. L. Seyler, D. Zhong, E. Schmidgall, M. A. McGuire, D. H. Cobden, W. Yao, D. Xiao, P. Jarillo-Herrero, X. Xu, *Nature* **2017**, *546*, 270.
[15] C. Gong, L. Li, Z. Li, H. Ji, A. Stern, Y. Xia, T. Cao, W. Bao, C. Wang, Y. Wang, Z. Q. Qiu, R. J. Cava, S. G. Louie, J. Xia, X. Zhang, *Nature* **2017**, *546*, 265.
[16] Y. Xu, A. Ray, Y.-T. Shao, S. Jiang, K. Lee, D. Weber, J. E. Goldberger, K. Watanabe, T. Taniguchi, D. A. Muller, K. F. Mak, J. Shan, *Nat. Nanotechnol.* **2022**, *17*, 143.
[17] Y. Deng, Y. Yu, Y. Song, J. Zhang, N. Z. Wang, Z. Sun, Y. Yi, Y. Z. Wu, S. Wu, J. Zhu, J. Wang, X. H. Chen, Y. Zhang, *Nature* **2018**, *563*, 94.
[18] K. S. Burch, D. Mandrus, J.-G. Park, *Nature* **2018**, *563*, 47.
[19] M. Wu, Z. Li, T. Cao, S. G. Louie, *Nat. Commun.* **2019**, *10*, 2371.
[20] Z. Wang, T. Zhang, M. Ding, B. Dong, Y. Li, M. Chen, X. Li, J. Huang, H. Wang, X. Zhao, Y. Li, D. Li, C. Jia, L. Sun, H. Guo, Y. Ye, D. Sun, Y. Chen, T. Yang, J. Zhang, S. Ono, Z. Han, Z. Zhang, *Nat. Nanotechnol.* **2018**, *13*, 554.
[21] B. Huang, G. Clark, D. R. Klein, D. MacNeill, E. N. Moratalla, *Nat. Nanotechnol.* **2018**, *13*, 544.

[22] S. Jiang, J. Shan, K. F. Mak, *Nat. Mater.* **2018**, *17*, 406.
[23] S. Jiang, L. Li, Z. Wang, K. F. Mak, J. Shan, *Nat. Nanotechnol.* **2018**, *13*, 549.
[24] T. Song, X. Cai, M. W.-Y. Tu, X. Zhang, B. Huang, N. P. Wilson, K. L. Seyler, L. Zhu, T. Taniguchi, K. Watanabe, M. A. McGuire, D. H. Cobden, D. Xiao, W. Yao, X. Xu, *Science* **2018**, *360*, 1214.
[25] Z. Wang, I. G. Lezama, N. Ubrig, M. Kroner, M. Gibertini, T. Taniguchi, K. Watanabe, A. Imamoğlu, E. Giannini, A. F. Morpurgo, *Nat. Commun.* **2018**, *9*, 2516.
[26] S. Jiang, L. Li, Z. Wang, J. Shan, K. F. Mak, *Nat. Electron.* **2019**, *2*, 159.
[27] T. R. Paudel, E. Y. Tsymbal, *ACS Appl. Mater. Interfaces* **2019**, *11*, 15781.
[28] P. Jiang, L. Li, Z. Liao, Y. X. Zhao, Z. Zhong, *Nano Lett.* **2018**, *18*, 3844.
[29] J. L. Lado, J. F. Rossier, *2D Mater.* **2017**, *4*, 035002.
[30] M. U. Farooq, J. Hong, *npj 2D Mater. Appl.* **2019**, *3*, 3.
[31] Y. Zhang, J. Liu, R. Deng, X. Shi, H. Tang, H. Chen, H. Yuan, *RSC Adv.* **2022**, *12*, 28533.
[32] J. Zhang, B. Zhao, T. Zhou, Y. Xue, C. Ma, Z. Yang, *Phys. Rev. B* **2018**, *97*, 085401.
[33] T. Song, Z. Fei, M. Yankowitz, Z. Lin, Q. Jiang, K. Hwangbo, Q. Zhang, B. Sun, T. Taniguchi, K. Watanabe, M. A. McGuire, D. Graf, T. Cao, J.-H. Chu, D. H. Cobden, C. R. Dean, D. Xiao, X. Xu, *Nat. Mater.* **2019**, *18*, 1298.
[34] C.-C. Tseng, T. Song, Q. Jiang, Z. Lin, C. Wang, J. Suh, K. Watanabe, T. Taniguchi, M. A. McGuire, D. Xiao, J.-H. Chu, D. H. Cobden, X. Xu, M. Yankowitz, *Nano Lett.* **2022**, *22*, 8495.
[35] G. Tenasini, D. S. Delgado, Z. Wang, F. Yao, D. Dumcenco, E. Giannini, K. Watanabe, T. Taniguchi, C. Moulsdale, A. G. Ruiz, V. I. Fal'ko, I. G. Lezama, A. F. Morpurogo, *Nano Lett.* **2022**, *16*, 6760.
[36] T. K. Chau, S. J. Hong, H. Kang, D. Suh, *npj Quantum Mater.* **2022**, *7*, 27.
[37] P. Wei, S. Lee, F. Lemaitre, L. Pinel, D. Cutaia, W. Cha, F. Katmis, Y. Zhu, D. Heiman, J. Hone, J. S. Moodera, C.-T. Chen, *Nat. Mater.* **2016**, *15*, 711.
[38] Y. Zhang, T.-T. Tang, C. Girit, Z. Hao, M. C. Martin, A. Zettl, M. F. Crommie, Y. R. Shen, F. Wang, *Nature* **2009**, *459*, 820.
[39] H. Yang, J. Heo, S. Park, H. J. Song, D. H. Seo, K.-E. Byun, P. Kim, I. Yoo, H.-J. Chung, K. Kim, *Science* **2012**, *336*, 1140.
[40] J.-H. Lee, D. H. Shin, H. Yang, N. B. Jeong, D.-H. Park, K. Watanabe, T. Taniguchi, E. Kim, S. W. Lee, S. H. Jhang, B. H. Park, Y. Kuk, H.-J. Chung, *Nat. Commun.* **2021**, *12*, 1000.
[41] D. R. Klein, D. MacNill, J. L. Lado, D. Soriano, E. N. Moratalla, K. Watanabe, T. Taniguchi, S. Manni, P. Canfield, J. F. Rossier, P. J. Herrero, *Science* **2018**, *360*, 1218.
[42] H. H. Kim, S. Jiang, B. Yang, S. Zhong, S. Tian, C. Li, H. Lei, J. Shan, K. F. Mak, A. W. Tsen, *Adv. Mater.* **2020**, *32*, 1905433.
[43] D. Soriano, C. Cardoso, J. F. Rossier, *Solid State Commun.* **2019**, *299*, 113662.
[44] N. Sivadas, S. Okamoto, X. Xu, C. J. Fennie, D. Xiao, *Nano Lett.* **2018**, *18*, 7658.
[45] S. W. Jang, M. Y. Jeong, H. Yoon, S. Ryee, M. J. Han, *Phys. Rev. Mater.* **2019**, *3*, 031001.
[46] T. Ozaki, H. Kino, J. Yu, M. J. Han, M. Ohfuchi, F. Ishii, K. Sawada, Y. Kubota, Y. P. Mizuta, H. Kotaka, N. Yamaguchi, H. Sawahata, T. B. Prayitno, T. Ohwaki, T. V. Duy, M. Miyata, G. Jiang, T. Iitaka, P.-H. Chang, A. Terasawa, Y. Gohda, H. Weng, Y. Shiihara, M. Toyoda, Y. Okuno, R. Perez, P. P. Bell, M. Ellner, Y. Xiao, A. M. Ito, et al., source package for material explorer (www.openmx-square.org).
[47] J. P. Perdew, K. Burke, M. Ernzerhof, *Phys. Rev. Lett.* **1996**, *77*, 3865.
[48] S. Grimme, J. Antony, S. Ehrlich, H. Krieg, *J. Chem. Phys.* **2010**, *132*, 154104.
[49] S. Grimme, S. Ehrlich, L. Goerigk, *J. Comput. Chem.* **2011**, *32*, 1456.
[50] S. Grimme, *Comput. Chem.* **2006**, *27*, 1787.
[51] H. Chen, A. J. Millis, *Phys. Rev. B* **2016**, *93*, 045133.
[52] H. Park, A. J. Millis, C. A. Marianetti, *Phys. Rev. B* **2015**, *92*, 035146.
[53] S. Ryee, M. J. Han, *Sci. Rep.* **2018**, *8*, 9559.
[54] S. W. Jang, S. Ryee, H. Yoon, M. J. Han, *Phys. Rev. B* **2018**, *98*, 125126.
[55] S. Ryee, M. J. Han, *J. Phys.: Condens. Matter* **2018**, *30*, 275802.
[56] X. Kong, H. Yoon, M. J. Han, L. Liang, *Nanoscale* **2021**, *13*, 16172.
[57] A. I. Liechtenstein, M. I. Katsnelson, V. P. Antropov, *J. Magn. Magn. Mater.* **1987**, *67*, 65.
[58] H. Yoon, T. J. Kim, J.-H. Sim, S. W. Jang, T. Ozaki, M. J. Han, *Phys. Rev. B* **2018**, *97*, 125132.
[59] H. Yoon, T. J. Kim, J.-H. Sim, M. J. Han, *Comput. Phys. Commun.* **2020**, *247*, 106927.
[60] H. Yoon, S. W. Jang, J.-H. Sim, T. Kotani, M. J. Han, *J. Phys.: Condens. Matter* **2019**, *31*, 405503.
[61] M. J. Han, T. Ozaki, J. Yu, *Phys. Rev. B* **2004**, *70*, 184421.
[62] D. Ghazaryan, M. T. Greenaway, Z. Wang, V. H. G. Moreira, J. Yin, Y. Liao, S. V. Morozov, O. Kristanovski, A. I. Lichtenstein, M. I. Katsnelson, F. Withers, A. Mishchenko, L. Eaves, A. K. Geim, K. S. Novoselov, A. Misra, *Nat. Electron.* **2018**, *1*, 344.